



A space-forged super-thermal insulating material—lunar agglutinates



Ziwei Tian^{1,2,3,5}, Jie Zheng^{4,5}, Haidong Wang^{1,4,5} , Guang Zhang^{1,5} , Yanxi Chen^{1,4},
Ronghua Pang^{1,2}, Quan Zheng^{1,3}, Xin Liu¹, Songzheng Yu¹, Guanghui Liu¹, Yiwei Liu¹, Jianzhong Liu^{1,2},
Yang Li^{1,2} , Bingyang Cao⁴ , Peng Zhang¹ & Ziyuan Ouyang²

The development of high-efficiency thermal insulation materials is crucial for terrestrial and space applications under extreme conditions. Synthetic aerogels, featuring porosities up to 99%, can reach the values of $\sim 10 \text{ mW m}^{-1} \text{ K}^{-1}$ under vacuum. However, whether natural materials can achieve this performance remains an open question. Here, we report lunar agglutinates from the Chang'E-5 mission that exhibit thermal conductivities as low as $\sim 8 \text{ mW m}^{-1} \text{ K}^{-1}$ under vacuum, surpassing most high-performance aerogel materials — at modest porosities of only 7–30%. Integrated structural characterizations and atomic-to-mesoscale simulations demonstrate that the space-weathering-forged multiscale voids and multiphase interfaces collaboratively suppress phonon transport within agglutinate particles, leading to their ultra-low thermal conductivities. These natural structures demonstrate a non-porosity-dominated thermal insulation mechanism. The findings redefine the microstructural design principles for super-insulating materials and provide a particle-scale explanation for the ultralow thermal conductivity of lunar regolith.

The pursuit of materials with ultralow thermal conductivity has long been a major scientific objective, particularly for applications in extreme aerospace thermal protection, high-precision manufacturing, lunar and deep-space exploration^{1–6}. Among natural materials on Earth, pumice—formed through volcanic eruptions—exhibits a low thermal conductivity, on the order of $100 \text{ mW m}^{-1} \text{ K}^{-1}$ ^{7,8}. Through structural design and advanced fabrication, researchers have developed synthetic aerogels, which exhibit extremely high porosity and ultralow thermal conductivity. Under vacuum conditions, these materials can achieve thermal conductivities as low as $\sim 1\text{--}10 \text{ mW m}^{-1} \text{ K}^{-1}$ ^{1–5}. Under non-vacuum conditions, heat transfer in aerogel materials arises from the combined contributions of solid-phase conduction, gas-phase conduction, and thermal radiation, while convective heat transfer is effectively suppressed by their nanoporous structure⁶. Accordingly, optimization of thermal insulation in aerogels should primarily focus on weakening conductive and radiative heat transfer. Although increasing porosity can effectively reduce solid-phase thermal conduction, further enhancement of insulation performance through porosity maximization alone has become increasingly difficult. Unless mitigated by Knudsen effects or vacuum conditions, enlarged pore sizes can significantly enhance gas-phase heat conduction^{2,6}. Consequently, contemporary aerogel research has shifted toward microstructural and interfacial engineering

strategies, including reducing characteristic pore and strut dimensions, constructing complex and tortuous solid networks, and suppressing radiative heat transfer by introducing infrared-absorbing components, thereby achieving ultralow thermal conductivity beyond a porosity-dominated design paradigm^{4,5}. As artificial thermal insulating materials have continuously pushed the limits of achievable performance, an intriguing question arises: Does nature also host materials with comparably extreme or even superior thermal insulation that could inspire further advances in insulation design paradigms?

Direct in-situ measurements from Apollo missions and laboratory analyses of returned samples have revealed that lunar regolith exhibits extremely low thermal conductivity ($0.57\text{--}3.41 \text{ mW m}^{-1} \text{ K}^{-1}$), even an order of magnitude lower than man-made aerogels, making it an exceptional natural insulation material^{9–20}. While the primary constituents of regolith—such as pyroxene, olivine, and plagioclase—exhibit intrinsic thermal conductivity values ranging from 1.50 to $5.70 \text{ W m}^{-1} \text{ K}^{-1}$ ^{21–24}, the thermal conductivity of bulk regolith is suppressed by three orders of magnitude. This dramatic reduction demands resolution of its physical origins. Prevailing theories attribute the regolith's extremely low thermal conductivity to its highly porous, loosely packed structure under the high-vacuum lunar environment^{25,26}. However, it is noteworthy that synthetic aerogels, which

¹Technology and Engineering Center for Space Utilization, Chinese Academy of Sciences, Beijing, China. ²Center for Lunar and Planetary Sciences, Institute of Geochemistry, Chinese Academy of Sciences, Guiyang, China. ³University of Chinese Academy of Sciences, Beijing, China. ⁴Department of Engineering Mechanics, Tsinghua University, Beijing, China. ⁵These authors contributed equally: Ziwei Tian, Jie Zheng, Haidong Wang, Guang Zhang.

e-mail: hdwang@tsinghua.edu.cn; zhangguang@csu.ac.cn; liyang@mail.gyig.ac.cn; caoby@tsinghua.edu.cn; zhangpeng@csu.ac.cn

typically have a porosity ranging from 95 to 99%, significantly exceed the porosity of lunar surface regolith yet still fail to achieve its extreme thermal insulation. Moreover, their macroscopic packing structure cannot be compared with the deliberately engineered hierarchical solid networks and microscale pore structures designed in aerogels. This suggests that the superior insulating properties of lunar regolith involve factors beyond macroscopic porosity. Understanding the underlying microscopic mechanisms may provide new insights for developing innovative thermal insulation strategies in materials design.

The Moon's extreme environment—characterized by high vacuum, intense radiation, micrometeorite impact, and severe thermal cycling—drives

exogenic geological processes that forge the morphology and composition of lunar regolith across scales, from individual grains to macrostructure. It is under these conditions that space weathering, primarily through solar wind implantation, micrometeorite impacts, and cosmic ray irradiation, continuously modifies the lunar surface, generating regolith composed of complex particles including glassy beads, rock fragments (e.g., basaltic and mineral fragments), and agglutinates (AGG.)^{27,28} (Fig. 1a). Most specially, the lunar agglutinates are exclusively formed through space weathering. Their unique formation processes and heterogeneous porous nano- to microscale architectures may result in remarkably low thermal conductivity, making them a critical factor in the thermal insulating properties of lunar regolith.

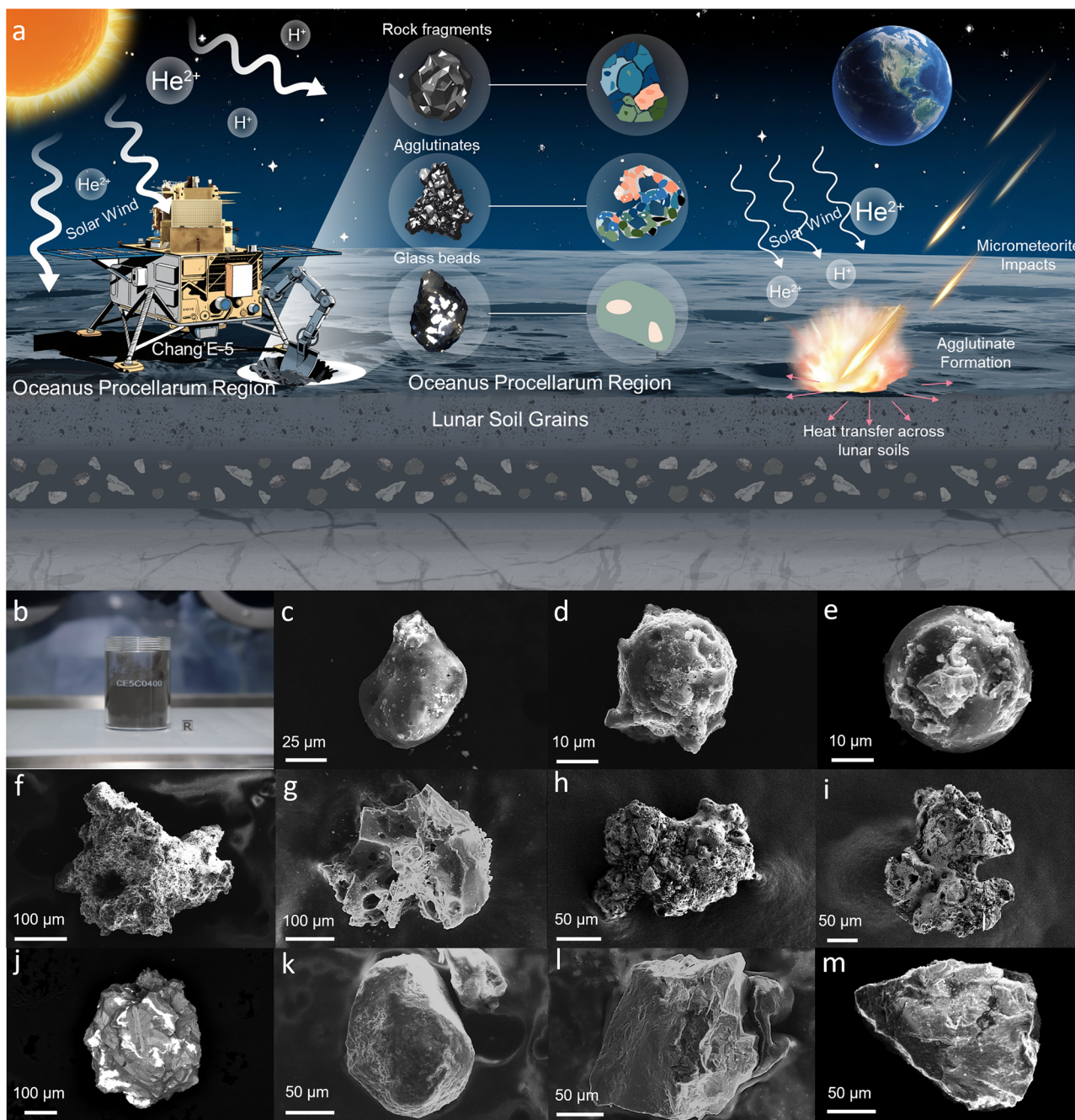


Fig. 1 | Complex surface morphology in lunar regolith particles induced by space weathering processes. **a** Morphological diversity of CE-5 regolith particles shaped by micrometeorite impacts and solar wind irradiation. Particles are classified by appearance and structure: glass beads, agglutinates (highest complexity), and rock

fragments (basaltic debris). **b** Airtight curation for pristine CE-5 samples. **c–e** Scanning electron microscopy (SEM) analysis of representative glass beads (GLASS #1–3). **f–i** Agglutinate particles (AGG. #1–4) exhibiting melt matrices and embedded mineral fragments. **j–m** Rock fragments (ROCK #1–4).

Here, we report the first precise thermal conductivity measurements of individual lunar regolith particles returned by the Chang'E-5 mission. We identify lunar agglutinate as a natural material exhibiting exceptionally low thermal conductivity, with values measured as low as $\sim 8 \text{ mW m}^{-1} \text{ K}^{-1}$ under vacuum using a suspended thermal bridge method with an H-type sensor, approaching the performance of artificial aerogel-based thermal insulators. Structural characterization and first-principles calculations confirm that this extreme thermal insulation originates from the unique space-weathered architecture of agglutinate, in which multiscale defects and complex interfaces collectively suppress heat transport.

Results and discussion

The formation and morphology of lunar regolith particles

The Chang'E-5 (CE-5) mission returned approximately 1731 g of lunar samples from a landing site situated in the northeastern part of Oceanus Procellarum (51.916°W, 43.058°N), which corresponds to the youngest volcanic basalt unit ever sampled on the Moon^{29,30}. Analyses confirm CE-5 samples are dominated by a large amount of rock fragments (basaltic and mineral fragments), with 11.6–20.0% glassy substance (including glass beads and amorphous substances in agglutinates)^{31–33}. Particle size distributions span broadly (median diameter: $\sim 55.24 \mu\text{m}$)^{32,33}, reflecting pronounced space weathering effects such as micrometeorite impacts and solar wind sputtering³⁴ (Fig. 1). In this work, we have sorted 11 representative CE-5 lunar regolith particles, including 4 agglutinates, 4 rock fragments, and 3 glass beads. These particles were derived from the homogenized surface samples (CE5C0400YJFM00402H, Fig. 1b), taken by surface shovel after mixing. The regolith exhibits a particle size distribution of 4.84–432.27 μm (median: 52.54 μm , mean: 49.80 μm ; 95% mass fraction), with mineralogy dominated by pyroxene ($\sim 42\%$), feldspar ($\sim 30\%$), glass ($\sim 16.6\%$), olivine ($\sim 5.7\%$), and ilmenite (4–5%)³³. Scanning electron microscopy (SEM) analysis reveals three morphologically distinct particle classes: glassy beads (Fig. 1c–e) exhibit smooth spheroidal or ellipsoidal morphologies with sharply defined edges. Agglutinates (Fig. 1f–i) display irregular, amorphous microtextures and diffuse boundary regions³⁴. Rock/mineral fragments (Fig. 1j–m) exhibit distinct angular morphologies with clear edges and visible cleavage planes³⁵. Mineral fragments (Fig. 1l, m) possess sharper edges compared to rock fragments (Fig. 1j, k). These image results visually demonstrate a descending order of apparent geometric complexity among agglutinates, rock fragments, and glass beads.

X-ray computed tomography (X-CT) was employed to resolve and characterize the internal structures of three types of lunar particles. Combined with SEM-EDS analysis, this approach identified the principal mineral and amorphous phases present (Methods), thereby revealing the internal mineral phase distribution and multiscale pore architecture within individual lunar regolith particles. As a distinctive product of space weathering, agglutinates comprise mixtures of major lunar minerals—including plagioclase, pyroxene, olivine, and ilmenite—embedded within a glassy matrix (Fig. 2a). These form through impact melting induced by meteoritic and micro-meteoritic impact, which generates molten glass that envelops mineral fragments and creates complex interfaces between crystalline and amorphous phases, as well as between distinct crystals. Furthermore, gases liberated by the thermal decomposition of oxygen-bearing minerals in the regolith become entrapped during the rapid cooling and solidification of the melt. This process results in the formation of multiscale vesicles, ranging from nanometers to micrometers in size, within the agglutinate particles.

Rock fragments form primarily through the fragmentation of lunar bedrock caused by meteoritic impacts. Concurrently, extreme thermal cycling can induce internal thermal stress, leading to interfacial sliding or compression due to thermal expansion mismatch between mineral phases. This process generates intergranular or transgranular cracks (Fig. 2d). Their intact crystalline structure limits the presence of large pores ($> \text{tens of micrometers}$), making the fragments generally dense and coherent. Similar to agglutinates, rock fragments contain numerous mineral–mineral interfaces; however, these are predominantly well-crystallized intergrowth

boundaries. The total interfacial area is smaller than in agglutinates and entirely lacking crystal–amorphous interfaces (Fig. 2b). Lunar glass beads are mainly produced by rapid cooling of molten material generated by external dynamic processes. During ejection, they may undergo rotation and drag, which do not always result in perfect sphericity. Internally, the beads are generally homogeneous but can contain entrained mineral fragments or vesicles formed by trapped gas. For example, 3D reconstruction of GLASS#1 reveals a trailing end, two high-density metallic cores, and minor vesicles (Fig. 2c).

Among the three types of lunar regolith particles, agglutinates exhibited a significantly higher average porosity (17.78%) compared to rock fragments (4.02%) and glass beads (1.38%), as quantified from pores and microcracks (Fig. 2d). As described above, the morphological and mineralogical 3D reconstruction of particles confirms that the agglutinates exhibit intricate internal architectures with multiphase intergrowths, creating crystalline/amorphous interfaces and disordered multiscale porosity. This complexity leads to the presence of numerous multiphase interfaces, including both crystalline and crystal–amorphous types, as well as disordered multiscale pores within the particles (Figs. 2a and S1–S5). Furthermore, lunar regolith particles exhibit microstructural defects—including vesicles and nanopores—at scales exceeding tomographic resolution limits^{36–39}. Rock fragments and agglutinates share a common material origin; however, limited space weathering has not yet induced extensive fragmentation or reorganization within the fragments. As a result, they exhibit relatively simple interfaces and lack nano- to microscale defects and pores. In contrast, glass beads are structurally and compositionally simpler.

Intrinsic thermal conductivity of lunar regolith particles

We employed a custom-designed suspended H-type device^{40–42} (Fig. 3a, b) (Methods) to precisely measure the thermal conductivities of individual lunar regolith particles. The device integrates two independent gold nano-sensors (Sensor #1, #2) bridged by the test particle. The nano-sensors in the device serve both as a Joule heater and a precise resistance thermometer. All experiments were conducted in a high-vacuum environment (pressure $< 10^{-3} \text{ Pa}$) to avoid heat loss from the sample due to heat convection, while heat loss from radiation was also negligible.

The measurement results show that the κ values vary substantially across lunar particle types (Fig. 3c). Space-weathered agglutinates represent ultralow thermal conductivity ($\kappa \sim 8 \text{ mW m}^{-1} \text{ K}^{-1}$ at 253 K in vacuum, Fig. 3c), comparable to that of most artificial aerogels^{1–5}. The extremely low thermal conductivity of aerogels primarily stems from their abundant multiscale pore structures, strong phonon scattering at solid skeleton interfaces, and low substrate thermal conductivity¹. This also confirms that agglutinates' complex internal morphological and mineralogical features severely impede heat transport. Within the studied temperature range, the thermal conductivity of agglutinate slightly increasing with temperature (κ : AGG. #1: 8–17 $\text{mW m}^{-1} \text{ K}^{-1}$ from 253 to 413 K; Fig. 3c). Conversely, rock fragments (κ : ROCK #1: 36–27 $\text{mW m}^{-1} \text{ K}^{-1}$) and glass beads (κ : GLASS #1 150–120 $\text{mW m}^{-1} \text{ K}^{-1}$) display decreasing κ with rising temperature, plateauing at higher temperature. Glass beads exhibit a smaller relative variation in thermal conductivity with temperature compared to rock fragments. For non-metallic materials in which heat transport is dominated by phonons, thermal conductivity generally decreases with increasing temperature⁴³. However, in amorphous materials, the phonon mean free path is strongly limited by atomic disorder and is therefore nearly temperature independent⁴⁴, which weakens the influence of temperature on phonon transport. In addition, radiative heat transfer occurs between pores in porous materials and contributes to the effective thermal conductivity; as temperature increases, radiative effects become more significant, leading to an increase in the effective thermal conductivity. This behavior has also been observed in thermal conductivity measurements of consolidated porous rocks on Earth and in artificial thermally insulating aerogel materials^{3,45}. The observed increase in thermal conductivity with temperature in agglutinates may be jointly associated with their amorphous-rich chemical characteristics and their complex, highly porous structure. Particle size inversely

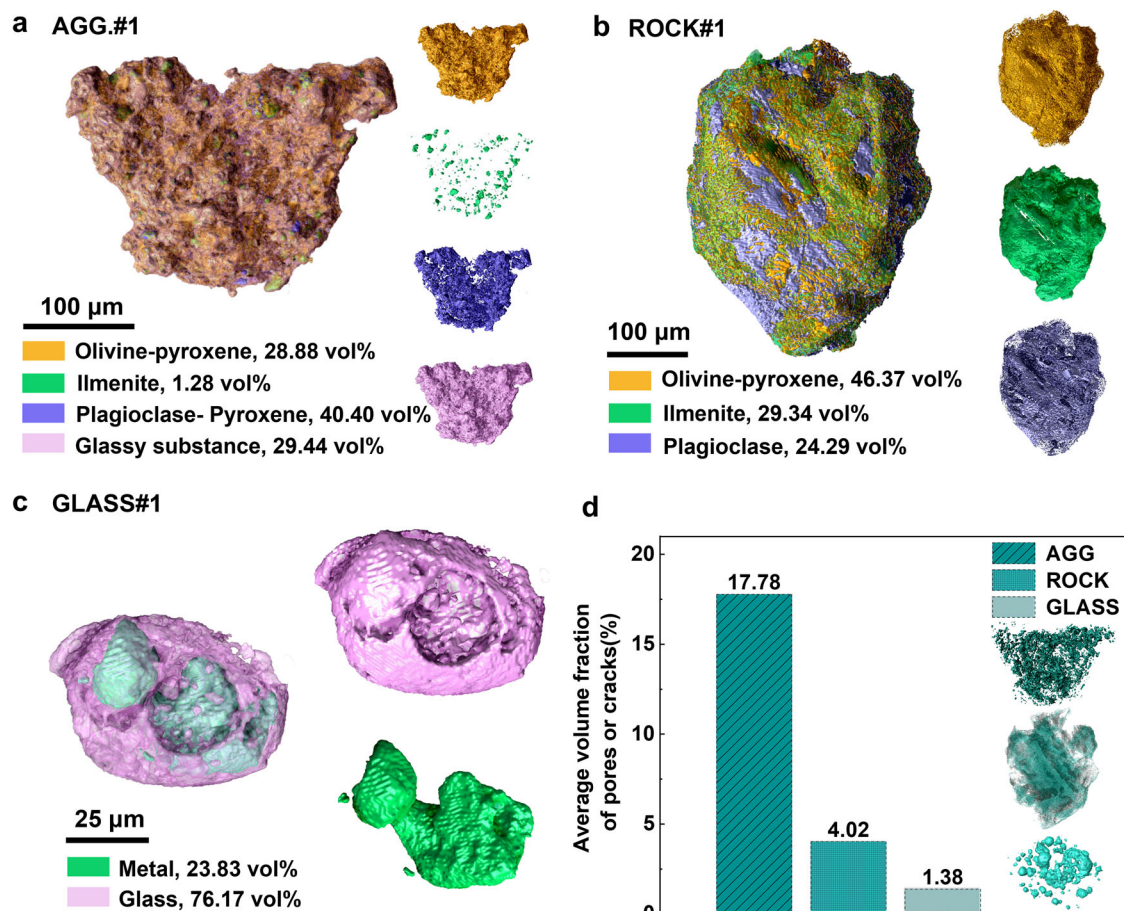


Fig. 2 | Three-dimensional reconstruction reveals the internal structure of lunar regolith particles. **a** 3D morphological and mineralogical reconstruction model of AGG. #1, showing mineral phases: Ol-Px (Calcium magnesium silicate, 28.88%), Pl-Px (40.40%), Ilm (1.28%), and glass (29.44%). **b** Reconstruction model of ROCK #1 with mineral phases: Ol-Px (46.37%), Pl (24.29%), and Ilm (29.34%).

c Reconstruction model of GLASS #1, consisting of a metallic core (23.83%) and glassy phase (76.17%). **d** Average volume fraction of pores or cracks in #1–#4 agglutinates (17.78%), #1–#4 rock fragments (4.02%), and #1–#3 glassy beads (1.38%). Mineral abbreviations: Ilm ilmenite, Ol olivine, Px pyroxene, Pl plagioclase.

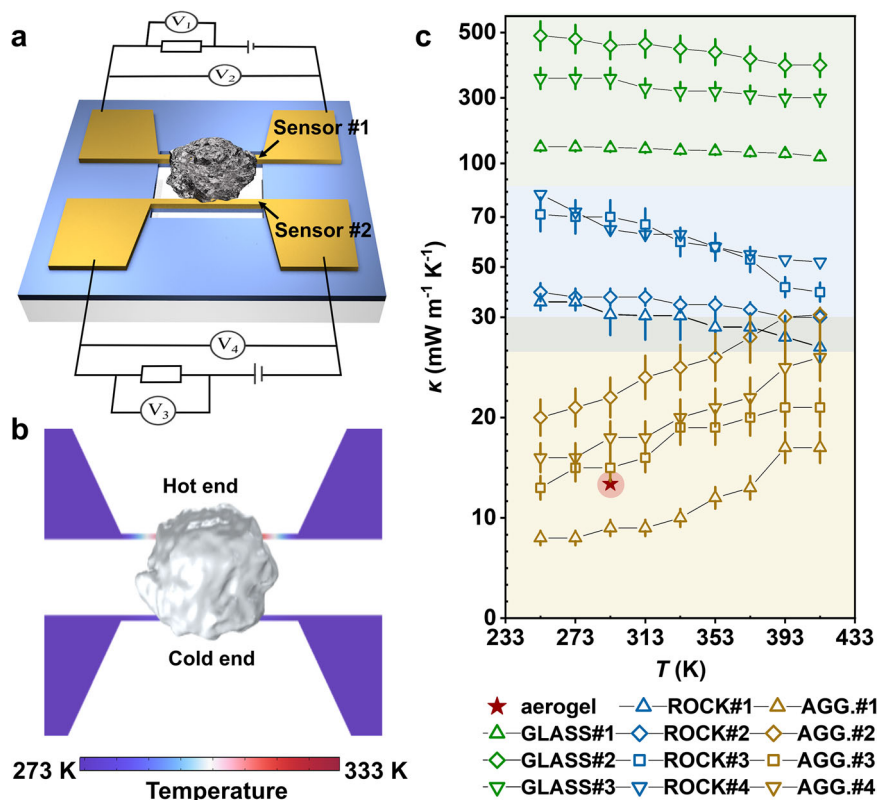
modulates thermal conductivity for all types, but sensitivity diverges markedly: crystallinity-dominated glass beads show strong size dependence, agglutinates and rock fragments remain stable across ~ 100 – $400 \mu\text{m}$ (Fig. S1a–c)—attributable to their disorder-dominated thermal buffering.

Agglutinate particles exhibit notably lower thermal conductivity than the rock fragments and glass beads (Fig. 3c). Microstructural analysis reveals the origin of this exceptional behavior: SEM imaging shows mineral fragments (plagioclase, pyroxene, olivine, etc.) agglutinated in a glassy matrix with high surface irregularity (Figs. S2–S5) (Methods), while X-CT (spatial resolution $\sim 0.7 \mu\text{m}$) and 3D reconstruction of particle disclose a disordered porous network (mean pore size: $6.20 \mu\text{m}$; porosity: 18.54%) in AGG. #1 (Figs. 2a and S6a) (Methods). This architecture maximizes phonon scattering through multiscale interfaces. Contrastingly, AGG. #2 displays higher porosity (28.50%) but larger, isolated pores (mean pore size: $13.39 \mu\text{m}$; Fig. S6b) and simpler composition dominated by glass-bonded limited mineral fragments, which yields higher average thermal conductivity ($\kappa \sim 20 \text{ mW m}^{-1} \text{ K}^{-1}$), confirming that the pore connectivity and morphological complexity—not solely porosity—govern thermal transport suppression. AGG. #3 and #4 share the fundamental amorphous melt-bonded structure of AGG. #1 (Figs. S4, S5 and S6c, d). Despite differing porosities (AGG. #3–7.75% and AGG. #4–16.31%, respectively), their thermal conductivities remain comparably low (AGG. #3: $\kappa \sim 13 \text{ mW m}^{-1} \text{ K}^{-1}$; AGG. #4: $\kappa \sim 16 \text{ mW m}^{-1} \text{ K}^{-1}$), which are slightly higher than that of AGG. #1 and consistent with the agglutinates' intrinsic thermal insulating nature. This confirms ultralow κ as a universal property of space-weathered agglutinates,

governed by microstructural complexity rather than porosity alone. Crucially, agglutinates exhibit notably lower κ than other regolith particles: 3–5 times lower than the rock fragments and 10–100 times lower than the glass beads (Fig. 3c).

Thermal conductivity measurements reveal that both the rock fragments (27 – $79 \text{ mW m}^{-1} \text{ K}^{-1}$) and glass beads (120 – $490 \text{ mW m}^{-1} \text{ K}^{-1}$) possess significantly higher κ values than agglutinates. ROCK #1 exhibits the lowest κ (average: $\sim 31 \text{ mW m}^{-1} \text{ K}^{-1}$) due to its high-density cracks among rock fragments (Figs. 2b, d and S7), while ROCK #3 and #4—composed mainly of olivine and pyroxene (Figs. S8 and S9)—show higher values (~ 67 and $\sim 62 \text{ mW m}^{-1} \text{ K}^{-1}$, respectively), though still an order of magnitude lower than their terrestrial counterparts (Fig. S11) due to symbiotic mineral interfaces and internal cracks. ROCK #2 ($\sim 35 \text{ mW m}^{-1} \text{ K}^{-1}$, Fig. S10) also has lower thermal conductivity. Similarly, GLASS #1, an impact-derived glass with a metallic core (Fig. 2c) and $\sim 4.13\%$ porosity (Fig. S12; Table S1), has reduced κ ($\sim 120 \text{ mW m}^{-1} \text{ K}^{-1}$) resulting from interfacial phonon scattering and porosity. The thermal conductivity of GLASS #1 is reduced by a factor of 2–3 compared to the spherical volcanic glasses^{46,47} GLASS #2 and GLASS #3 ($\kappa \sim 460$ and $\sim 330 \text{ mW m}^{-1} \text{ K}^{-1}$, respectively; Figs. S13 and S14). The measurements of lunar rock fragments and glass beads demonstrate the significant influence of microstructure on thermal conductivity. Their thermal conductivity is considerably higher—by several times—than that of agglutinates, highlighting the distinctive thermophysical properties of agglutinates and underscoring the notable effect of the complex

Fig. 3 | Thermal conductivity characterization of lunar regolith particles. **a** Schematic of the suspended H-type device: V_1 and V_3 are designated for measuring the voltage across two standard resistors to determine the current in each circuit, while V_2 and V_4 measure the voltage applied to the two-gold nano-sensors. **b** COMSOL-simulated temperature distribution of the H-type device with particle sample at 273 K. **c** Temperature-dependent κ of agglutinates (8–31 $\text{mW m}^{-1} \text{K}^{-1}$, brown), rock fragments (27–79 $\text{mW m}^{-1} \text{K}^{-1}$, blue), and glass beads (120–490 $\text{mW m}^{-1} \text{K}^{-1}$, green) from 253 to 413 K. Here, a novel dome-celled aerogel material is presented, with a thermal conductivity of $\sim 13.4 \text{ mW m}^{-1} \text{K}^{-1}$ at room temperature and under vacuum conditions.



structures formed by space weathering on the thermal insulation properties of lunar agglutinates.

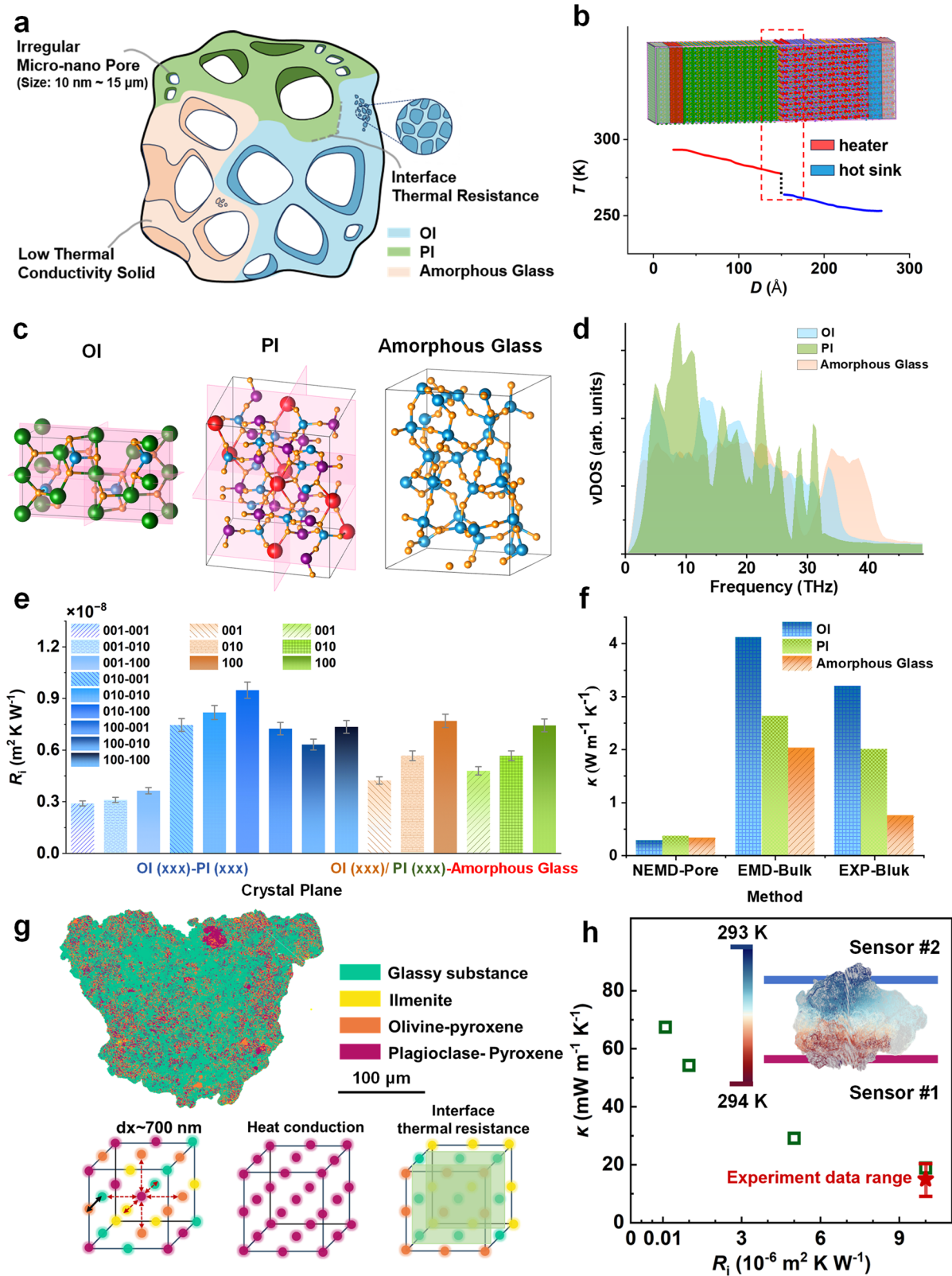
The influence of complex mineral interfaces on heat transfer

Based on the characterization of three-dimensional morphology/composition and structures, we investigated the formation mechanism of the intrinsic insulating properties of agglutinate particles using multiscale computational methods. The results reveal that their extremely low thermal conductivity is primarily attributed to the intense phonon scattering and high thermal resistance caused by complex micro-nanopores, and the thermal conductivities of internal phases is far lower than that of uniform and dense bulk materials (Fig. 4a). Using non-equilibrium molecular dynamics (NEMD)⁴⁸, the thermal resistance across the olivine (Ol), plagioclase (Pl) and amorphous glassy phase interfaces was systematically quantified (Methods). Taking the Pl-Ol interface as an example, the NEMD model and steady-state temperature distribution are shown in Fig. 4b: a temperature gradient was established across the system, and periodic boundary conditions were applied perpendicular to the direction of the temperature gradient. An amorphous model was constructed through a melt-quenching process of crystalline phase (Fig. 4c). The thermal resistance values were calculated for the combined interfaces of different crystalline planes of Ol, Pl and the amorphous glassy phase in Fig. 4c. The origin of interfacial thermal resistance can be well explained by the mismatch of vibration phonon modes on both sides of the interface, as shown in Fig. 4d. The vibrational density of states (vDOS) distributions of three substances differs significantly⁴⁹, and the discontinuity of the vibration modes leads to higher interfacial thermal resistance. The calculation results show (Fig. 4e) that the average interfacial thermal resistance under different crystalline ordination combinations is approximately $10^{-8} \text{ m}^2 \text{ K W}^{-1}$. Focused ion beam (FIB) and transmission electron microscope (TEM) characterization of the CE-5 lunar agglutinate particle reports that many pores, vesicles, and defects with sizes ranging from 10 to 150 nm exist^{36–39} (Fig. S15). High-magnification field-emission SEM further confirms the presence of abundant microscale pores and defects smaller than 1 μm on the surfaces of lunar

agglutinate particles (Fig. S16), which are difficult to be clearly and accurately resolved at the resolution of X-CT. Considering factors such as the elongation of the heat flow path and the reduction of thermal conductivity cross-sectional area caused by nanoscale structures in a cubic micro-element model, the equivalent interfacial thermal resistance is estimated to be approximately $10^{-5} \text{ m}^2 \text{ K W}^{-1}$.

Additionally, an equilibrium molecular dynamics (EMD) method was used to calculate the thermal conductivity of Ol, Pl, and amorphous glassy phase inside a lunar regolith particle, which is based on the Green-Kubo theory of linear response^{49–51} (Methods). The calculated thermal conductivities of uniform and dense bulk materials (seen as the ideal bulk phases on Earth) at 273 K are generally consistent with the experimental results (Fig. S11f), proving the rationality of the crystalline potential energy model used in molecular dynamics (MD) simulations. Meanwhile, the NEMD method was used to calculate the thermal conductivity of material with complex nanopores and interfaces, simulating the scenario of actual lunar regolith particles (Methods). As shown in Fig. 4f, the presence of complex nanoscale pore structures reduces the thermal conductivity to roughly 12% of the value of the ideal bulk phase. It is convinced that the high-density nanopores and interfaces due to space weathering (solar wind, micro-meteorite impacts, etc.) (Fig. S15) and the structural heterogeneity (intracrystalline zoning, defects, etc.) are responsible for the reduced thermal conductivity of lunar agglutinate particles.

To further clarify the underlying mechanisms of ultralow thermal conductivity of lunar regolith particles, especially agglutinates, we developed a cross-scale model linking microstructural characteristics to macroscale thermal properties for AGG.#1 ($\kappa \sim 8 \text{ mW m}^{-1} \text{K}^{-1}$) (Fig. 4g). Based on the preceding conjectures and computational verifications, the theoretical values of thermal conductivity for single-phase minerals containing microdefects and interfacial thermal resistance were incorporated into the finite difference model (FDM) as validated parameter inputs. Figure 4h shows the calculated κ of AGG.#1 under different interfacial thermal resistance conditions. Clearly, the thermal conductivity of the agglutinate particle decreases with the increase in the interfacial thermal resistance, and



good agreement between the calculated κ and the experimental value is obtained when the interfacial thermal resistance is approximately $10^{-5} \text{ m}^2 \text{ K W}^{-1}$. It is also noted that the calculated κ is slightly higher than the experimental data, because the macroscale thermal conductivity calculation model cannot fully resolve nanoscale defects and multiphase doping effects that further suppress conductivity in natural samples.

In this study, the heat transport properties of individual lunar regolith particles were systematically characterized under high-vacuum conditions and temperatures approximating those of the lunar surface, establishing an important experimental baseline for understanding intrinsic thermal transport at the particle scale. It should be further noted, however, that the actual lunar surface environment is considerably more complex than the

Fig. 4 | Microscale mechanisms of ultralow thermal conductivity in lunar regolith particles. **a** Schematic of hierarchical thermal suppression in agglutinates, combining nanoscale interfacial thermal resistance and micro-nanoscale porosity effects. **b** Non-equilibrium molecular dynamics (NEMD) simulation of plagioclase-olivine (Pl-Ol) interface. The constant-temperature heat source and hot sink are set to form a temperature gradient in the model, where the distance between the heat source/sink and the interface is controlled at approximately 10 nm. **c** Crystallographic models of olivine/pyroxene (Ol/Px), plagioclase (Pl), and amorphous glassy phase, with major crystal planes highlighted in red. **d** Vibrational density of states (vDOS) demonstrating phonon mode mismatch between different phases. **e** Calculation results of thermal resistance for various interfaces formed by the combination of different crystal planes of Ol/Px, Pl, and amorphous glassy phase at 273 K. The (xxx)

on the horizontal axis corresponds to the crystal planes in the legend. R_i represents the interfacial thermal resistance (ITR). **f** Comparison of thermal conductivities of Ol/Px, Pl, and amorphous glassy phase by three methods: NEMD (nanopores) vs. EMD (ideal bulk) vs. experiment, revealing several orders of thermal suppression in natural samples. **g** A finite difference heat conduction model constructed based on AGG. # 1 with mineral distribution (represented by discrete points with a spacing of 700 nm for the continuous materials). If a discrete point and its nearest-neighbor grid points (defined as the six adjacent points separated by the distance dx) share the same material composition, it is seen as bulk. If the discrete points and adjacent points are composed of different materials, the interfacial thermal resistance (ITR) exists. **h** Calculated thermal conductivity associated with ITR.

approximate lunar conditions employed in laboratory measurements. Continuous solar-wind proton implantation and space irradiation give rise to photoelectric-effect-driven electrostatic charge accumulation in insulating regolith materials⁵², as well as potential near-surface water formation processes^{53–55}. Together, these processes constitute a highly coupled and dynamically evolving system involving both physical and chemical processes. How these in-situ coupled multiphysics environmental fields further modulate the microscopic intrinsics and particle contact of lunar regolith particles, thereby affecting their thermal response, remains to be studied. The intrinsic thermal property data obtained in this work, together with the associated analyses of heat transfer mechanisms, therefore provide a foundation for future integrated studies that combine laboratory-based sample analysis with solar wind environment simulations and charged particle irradiation, enabling a more comprehensive understanding of the thermal evolution and governing physical mechanisms of lunar regolith particles under realistic space conditions.

Conclusions

In conclusion, lunar agglutinates from the Chang'E-5 mission exhibit exceptionally low thermal conductivity, with values reaching $\sim 8 \text{ mW m}^{-1} \text{ K}^{-1}$ under vacuum, comparable to those of most high-performance synthetic super-insulating aerogels, despite their relatively limited porosity (7–30%). The results show that this superior insulation stems from the collaborative effect of multiscale voids and multiphase interfaces formed by space weathering, which effectively block heat transfer by phonons. Importantly, these natural structures reveal a thermal insulation mechanism that does not rely solely on high porosity. This insight establishes a new paradigm for designing ultra-thermal-insulating materials that transcend conventional porosity-based approaches, rooted in the recognition that space weathering generates the Moon's exceptionally insulating regolith. This study also provides particle-scale insights into the formation mechanisms underlying the ultralow thermal conductivity of lunar regolith.

Methods

Optical microscope analysis

Stereomicroscope images of 11 tested particles were obtained using the ZEISS Smartzoom 5 optical microscope under the illumination of circular light.

Scanning electron microscopy (SEM) and energy dispersive spectrometer (EDS)

The chemical, elemental, and material composition of lunar regolith particles was qualitatively assessed using an SEM combined with energy dispersive spectroscopy (EDS). To ensure that the samples remained undamaged and uncontaminated, the ZEISS Gemini-500 was utilized to acquire secondary electron (SE) images and perform EDS at an accelerating voltage of 20 kV without any conductive coating. This method ensured that heavy elements, such as titanium (Ti) and iron (Fe), in the lunar regolith could be effectively excited and identified.

Focused ion beam (FIB) and transmission electron microscope (TEM)

The lamella of the interesting area was extracted using a FIB with an FEI Scios dual beam system. To obtain detailed insights into space weathering phenomena and accurately characterize each mineral phase, the FIB lamella was analyzed using a TEM with an FEI Talos F200X FE-STEM operating at 200 kV. The chemical composition of the lamella was analyzed using an EDS detector on the STEM instrument.

X-ray computed tomography (X-CT)

X-CT of the lunar regolith particles' morphology and internal structure was conducted using the ZEISS Xradia 510 X-CT system. With a spatial resolution of 700 nm, thousands of X-ray images were captured for each particle from various angles. To ensure clear imaging, the average imaging time for each particle was no less than 3 h, with an exposure time of 3 s per frame. The scanning voltage was set at 50 kV, and the power was maintained at 4 W. Combined with EDS analysis, various phase components within the lunar regolith particles were segmented based on image grayscale values. The relative volume fractions of different phases and the internal porosity of some complex particles were calculated.

Based on the SEM characterization results, a quantitative analysis (in terms of volume fraction and porosity) of the mineral phase and internal structure of the X-CT reconstruction was conducted (Fig. S17):

1. X-CT was employed to capture multi-angle X-ray images and reconstruct the microscopic geometric structure of lunar regolith particles. By leveraging the differences in X-ray penetration capabilities among various materials, minerals with distinct densities and their spatial distribution were identified.
2. The primary elemental distribution on the surface of lunar regolith particles was identified using SEM-EDS analysis, and the main mineral components were inferred accordingly.
3. Based on the mineral composition and density, mineral phase identification was conducted on the various grayscale regions identified by X-CT. A three-dimensional model was reconstructed to visualize their spatial distribution.

Suspended thermal bridge method

We employed suspended H-type sensors for thermal measurements^{40–42} (Fig. S18) (Video S1), combining joule heating and resistance thermometry. Nano-sensors were fabricated on 500 μm Si wafers with 50 nm Si_3N_4 layers: 100 nm Au nanosensor patterns were deposited using a 10 nm Cr adhesion layer, followed by selective etching to suspend structures and minimize substrate heat loss. Customized sensor geometries matched individual particle dimensions. A dual-robotic-arm transfer platform (2 μm -tip manipulators) integrated with optical microscopy enables precise particle placement. One arm positioned samples onto sensors using vacuum tweezers, while another stabilized particles with microprobes. Full suspension from the Si substrate ensured thermal isolation, enhancing measurement sensitivity.

Prior to measuring the thermal conductivity of the sample, the temperature coefficients of resistance (TCR) of both nano-sensors were

carefully calibrated. The ambient temperature of the experimental setup was precisely controlled by using a thermoelectric heating and cooling stage (INSTECH, TP102SV-PM-F8, ±0.001 K). By fine-tuning the electrical power delivered to the nanosensor and conducting a fit of the resistance-power curves, the resistance at zero power, which corresponds to the resistance at the ambient temperature, was ascertained through extrapolation. After that, the TCR was determined by altering the ambient temperature and performing a fit of the resistance-temperature curves.

In the experiment, Sensor #1 served as the “heater”, with a larger current applied to it in order to generate heat. Meanwhile, Sensor #2, to which a smaller current was applied with negligible heating effect, functioned as the “temperature detector”. The Joule heat produced by Sensor #1 was conducted through the sample to Sensor #2, resulting in temperature increases in both sensors. The temperature rise was precisely measured by keeping track of the resistance changes in both sensors by means of a four-wire method. By varying the heating power of Sensor #1 and fitting the temperature curves of both sensors, the temperature response coefficient (α) was obtained. Physically, α represents the temperature increase in Sensor #2 per 1 K increase in Sensor #1. Finally, a steady-state finite element model was established in COMSOL Multiphysics software to calculate the thermal conductivity of the particle sample. Experimental data of heating powers, thermal conductivities, and temperature rises of two sensors were used as input parameters, while the thermal conductivity of individual lunar soil particles was the only unknown parameter to be determined.

To confirm the measurement accuracy under the present experimental conditions, a micrometer-scale PEEK particle with a known thermal conductivity value was tested using the same measurement system (Fig. S19a). The thermal conductivity measured for PEEK agrees well with reported literature values (Fig. S19b)⁵⁶, confirming the reliability of the method for micrometer-scale particles, particularly those with low thermal conductivity. This validation provides a basis for the test of the intrinsic thermal conductivity of lunar regolith particles.

Details on the historical evolution of this measurement method and its reliability for measuring materials with extremely low thermal conductivity are provided in the “Supplementary Materials”.

Uncertainty analysis for the suspended thermal bridge method

The following factors are considered as the major sources of measurement uncertainties.

Uncertainty of the steady-state finite element model

COMSOL Multiphysics software was used to perform a finite element calculation for determining the thermal conductivity of a single lunar regolith particle. The grid independence of the finite element calculation model has been verified. Results indicate that the uncertainty in the calculation outcomes caused by grid density is less than 0.1%. Furthermore, the thermal conductivity values associated with the gold nanosensor and the Si₃N₄ layer were pre-calibrated, which led to an uncertainty of approximately 2% in the steady-state finite element model.

Uncertainty of thermal radiation

According to the Stefan–Boltzmann thermal radiation equation, the radiative heat transfer between the tested particle sample and the environment is:

$$J_r = \varepsilon_s \sigma A_s (T_s^4 - T_0^4) + \varepsilon_n \sigma A_n (T_n^4 - T_0^4) \quad (1)$$

where ε_s , A_s , and T_s are the emissivity coefficient, surface area, and temperature of the sample, respectively; ε_n , A_n , and T_n are the emissivity coefficient, surface area, and temperature of nanosensor, respectively; σ is the Stefan–Boltzmann constant ($5.67 \times 10^{-8} \text{ W m}^{-2} \text{ K}^{-4}$); and T_0 is the ambient temperature. The surface areas of the gold nano-sensors and particle sample are approximately 8×10^{-9} and $5 \times 10^{-8} \text{ m}^2$, respectively. The emissivities of the particle and nanosensor are considered as 0.8⁵⁷ and 0.1⁵⁸ from literature, respectively. The maximum temperature difference between the sensor/

particle and environment was 50 K in the experiment, so the radiative heat transfer can be estimated as $J_r = 10 \mu\text{W}$. The electric heating power of the sensor was about 150 μW . Therefore, the uncertainty caused by thermal radiation is approximately 6.7%.

Influence of contact thermal resistance

The contact thermal resistance between gold nano-sensors and micrometer-sized single particles has been measured in our previous work, approximately $6.2 \times 10^{-6} \text{ m}^2 \text{ K W}^{-1}$ ⁴². The thermal resistance of a single lunar agglutinate particle is calculated as $L/\kappa A = 4.1 \times 10^5 \text{ K W}^{-1}$, where L , κ , and A are the distance between two sensors, thermal conductivity, and average cross-sectional area of particle, respectively. Considering the contact area between sensors and the tested particle as approximately 300 μm^2 based on the optical microscopy image, the contact thermal resistance is less than 5% of the total thermal resistance of the particle sample. Actually, the contact thermal resistance has been taken into account in the FDM of thermal analysis as the boundary condition. Hence, the influence of contact thermal resistance is not considered as uncertainty in the current work.

Uncertainty of electrical measurement

A Keithley 2002 high precision multimeter with 8.5 digits precision was employed for voltage measurement, ensuring that the uncertainty of voltage measurement was less than 0.01%. The measurement expression of the temperature coefficient of resistance (β_T) is:

$$\beta_T = \frac{\Delta R_e}{R_e \Delta T} \quad (2)$$

with the error transfer formula, the uncertainty can be calculated as:

$$\frac{\delta\beta}{\beta} = \sqrt{\left(\frac{\delta\Delta R_e}{\Delta R_e}\right)^2 + \left(\frac{\delta R_e}{R_e}\right)^2 + \left(\frac{\delta\Delta T}{\Delta T}\right)^2} = \sqrt{2\left(\frac{\delta R_e}{R_e}\right)^2 + \left(\frac{\delta\Delta T}{\Delta T}\right)^2} \quad (3)$$

The temperature control module of the experimental platform exhibits a high degree of accuracy, with the capability to maintain temperature variations at an ultra-fine scale of 0.001 K. This level of precision is translated into a minimal uncertainty of less than 0.1% for the calibrated resistance temperature coefficient. By thoroughly considering the multiple sources of uncertainty, the total uncertainty in the measurement of thermal conductivity is estimated to be less than 9%.

Thermal conductivity calculation of AGG. #1 based on the finite difference method (FDM)

A discrete nodal network model of AGG. #1 was constructed using the distribution of mineral phases (reconstructed by X-CT), interface thermal resistance (calculated through MD), and measured thermal conductivities of monomineralic samples. The thermal properties of the internal phases were calibrated, and areas devoid of substances were designated as vacuum pores. Numerical simulations employed the conservation of energy and thermal boundary conditions with temperature gradients, solving steady-state temperature fields using the conjugate gradient method. The effective thermal conductivity of AGG. #1, which had multiphase interfaces and complex pore structures, was calculated using the heat flux integral across the cross-section and the specified boundary conditions.

To determine the thermal conductivity of porous particles numerically, the steady-state temperature field was first established by solving the heat conduction equation. Subsequently, the heat flux in a specified direction was calculated based on this temperature field and the thermophysical properties of the particles to obtain the equivalent thermal conductivity. The

steady-state heat conduction equation can be expressed as:

$$\nabla \cdot \left(\frac{1}{R} \nabla T \right) = 0 \quad (4)$$

where $T(\vec{x}, t)$ is the temperature at position x and time t , $R(\vec{x})$ represents the measured thermal resistance of constituent minerals in lunar regolith at position x .

The computational domain was uniformly discretized into N nodes with a spacing of dx (representing unit length here). For any node, the discretized equation can be expressed as:

$$\sum_j \frac{T_i - T_j}{\frac{dx}{2} (R_i + R_j) + R_{ij}} = 0, i = 1, 2, \dots, N \quad (5)$$

where j represents any adjacent node to i , R_{ij} denotes the interfacial thermal resistance obtained from MD simulations.

The particle ends were designated as the heat flux inlet (node set) and outlet (node set), with constant temperature boundary conditions applied.

$$T_i = T_{input}, i \in I \quad (6)$$

$$T_i = T_{output}, i \in O \quad (7)$$

The discretized system was solved using the conjugate gradient method. After obtaining the temperature field, the total heat flux Q was calculated by integrating over the particle's cross-sectional area. The equivalent thermal conductivity (κ_{eff}) was then derived as follows:

$$\kappa_{eff} = \frac{Q}{L(T_{input} - T_{output})} \quad (8)$$

where L is the actual path length of the heat flow from the high-temperature inlet (I) to the low-temperature outlet (O).

Additional calculations were performed to evaluate the temperature dependence of the thermal conductivity of agglutinates, which exhibit trends consistent with the experimental observations (Fig. S20). It should be further noted that the computational model primarily accounts for heat-transfer impediments arising from structure, interfaces, and porosity, while radiative heat transfer between pores is not included; consequently, the temperature-dependent increase predicted by the model is less pronounced than that observed experimentally. The numerical approach is based on constructing a discrete point set consistent with the phase composition and internal pore structure of agglutinates and solving heat transfer using a finite-difference method. The model parameters are derived from independent atomistic-scale property calculations, which inevitably lead to some deviation from experimental measurements. Moreover, higher-resolution characterizations (Figs. S15 and S16) reveal that the actual microstructure of lunar particles is considerably more complex than that represented in the finite-difference model. As a result, the calculated thermal conductivity values are slightly higher than the measured average effective thermal conductivity at each temperature; nevertheless, the calculated results remain within the measured range of AGG. #1 (Fig. 4h). Overall, the numerical calculations provide a description of the micro- to mesoscale heat-transfer impediment effects in lunar agglutinates.

Molecular dynamics (MD) simulation

The MD calculations were performed using the Large-scale Atomic/Molecular Massively Parallel Simulator^{59,60}. For Ol and Pl, the interactions between atoms within each phase were described by the CLAYFF potential⁶¹, which includes a Lennard-Jones (L-J) function and a Coulombic term. For the amorphous glassy phase, an amorphous model was obtained by firstly melting crystalline silica at a high temperature of 7000 K

and then rapidly cooling it to room temperature. The interatomic interactions in amorphous glassy phase were described by the BKS potential^{62,63}, which includes the Buckingham potential with a long-range Coulombic term. During the melt-quenching process, atoms approach each other closely, and the BKS potential cannot handle interatomic repulsive forces⁶⁴⁻⁶⁶. To ensure the correct description of cohesive forces during quenching, an L-J potential was added to the atoms in the amorphous glassy phase by referencing the L-J term in CLAYFF potential⁶⁶. The density of the fully relaxed amorphous glassy model is 2.21 g/cm³, which is consistent with that of amorphous silica. This result validates the rationality of the hybrid potential employed. For the interactions between atoms of different phases (Ol, Pl, or amorphous glass), the L-J potential was used to characterize the interfacial properties.

NEMD method was used to analyze the interfacial thermal resistance. If there is a temperature difference ΔT across the interface, and q is the heat flux density in the model, then the interfacial thermal resistance R can be calculated as Kapitza thermal resistance:

$$R = \frac{\Delta T}{q} \quad (9)$$

After modeling, the whole system was grouped in the isothermal-isobaric ensemble (NPT) to reach the thermal equilibrium at a temperature of 273 K and a pressure of 0 atm with the Nose-Hoover thermostat⁶⁷, allowing the interface between the two phases to form naturally. Subsequently, the whole system was converted to the microcanonical ensemble (NVE) with the Langevin thermostat set in the region of the heater and hot sink, with the heater maintained at 293 K and the hot sink at 253 K, where the distance between the heater and the hot sink was controlled at approximately 15 nm. The temperature difference between the heater and hot sink was sufficiently large to ensure a significant heat flux in the model, thereby minimizing errors caused by energy drift while remaining within the experimentally observed temperature range. The simulation employs a time step of 1 fs. After the temperature reaches equilibrium, the temperature distribution and heat flux density over a 2 ns time interval are extracted for calculating the thermal resistance at the interface.

In the calculation of homogeneous dense bulk materials, an EMD method was used to obtain the thermal conductivity components in different directions according to the Green-Kubo formula:

$$\kappa_\alpha = \frac{V}{k_B T^2} \int_0^\infty \langle J_\alpha(0) J_\alpha(t) \rangle dt \quad (10)$$

where V is the model volume, k_B is the Boltzmann constant, T is the temperature of the model, $J_\alpha(t)$ represents the time-dependent heat flux density in the α th direction, and $\langle \cdot \rangle$ means to calculating the ensemble average. The thermal conductivity of the homogeneous dense bulk material can be calculated as:

$$\kappa = \frac{1}{3} (\kappa_1 + \kappa_2 + \kappa_3) \quad (11)$$

EMD calculations were performed at 273 K. The size of the simulation box was controlled at approximately 15 nm, while the periodic boundary conditions were applied in all directions. Figure S21a-c shows the plots of the heat current autocorrelation function (HCACF) for the Ol, Pl, and amorphous glassy phase models. The convergence of the HCACF to zero ensures the accuracy of the thermal conductivity calculation results. Figure S21d-f is the schematic diagrams of the convergence of thermal conductivity with simulation time. The simulation employs a time step of 1 fs with a total simulation time of 6 ns.

Considering the influence of Nanopores on the thermal conductivity of materials, models of each phase with interlaced pores were established as shown in Fig. S22, and the NEMD method was used to calculate their thermal conductivity. In the heat transfer direction, atoms at both ends of

the model were fixed, and a constant-temperature heater and hot sink were constructed to form a temperature gradient in the model, where the distance between the heater and the hot sink was controlled at approximately 10 nm; in the directions that were perpendicular to the heat transfer direction, periodic boundary conditions were applied.

The thermal conductivity can be calculated according to Fourier's law of heat conduction as:

$$\kappa = -\frac{q}{\nabla T} \quad (12)$$

where q is the heat flux density, and ∇T is the temperature gradient in the heat transfer direction. After modeling, except for setting the temperature of the heater to 278 K and the hot sink to 268 K, all other calculation procedures and configurations are exactly the same as those for the interfacial thermal resistance calculation.

Equivalent interfacial thermal resistance model

Due to the limited scanning precision of X-CT technology, the sub-micron scale details cannot be represented in the model. Electron microscopy characterization of the CE-5 samples shows that the lunar agglutinate particles contain numerous defects, pores, and interfaces with sizes ranging from 10 to 150 nm^{36–39}. However, the X-CT model represents these features at this scale as a homogeneous dense single-phase material, with an identifiable interface density of 0.65 per μm^3 . To make the finite difference thermal analysis more consistent with reality, it is necessary to incorporate the nanoscale defects, pores, and interfaces, which are not identified by the X-CT model, into the identifiable interfaces as equivalent thermal resistance.

To crudely establish an equivalent thermal resistance model based on the identifiable interface density, consider a cubic micro-element with side length $d = 1.16 \mu\text{m}$ in the X-CT model, and its thermal resistance is calculated as:

$$R = \frac{d}{\kappa A} + \frac{R_e}{A} \quad (13)$$

where $A = d^2$ is the cross-sectional area for heat flow, and R_e is the equivalent interfacial thermal resistance. Based on NEMD calculations of the thermal conductivity of each phase with interlaced pores, the average thermal conductivity of the material is assumed to be $0.1 \text{ W m}^{-1} \text{ K}^{-1}$. Based on the electron microscopy characterization of the CE-5 samples, the cubic micro-element model is assumed to be composed of pores and single-phase particles of identical size. For simplicity, the cubic model is discretized into a uniform $10 \times 10 \times 10$ grid, where each cell represents either a single-phase particle or a pore. According to NEMD calculation results, the interfacial thermal resistance between two solid phases and porosity are assumed to be $10^{-8} \text{ m}^2 \text{ K W}^{-1}$ and 20%, respectively.

The heat conduction in the cubic micro-element model is analyzed as follows. First, the corresponding number of grid cells is randomly set as pores, while the remaining cells represent single-phase particles. Second, starting from the heat flow input surface, possible paths are constructed to enable the heat flow to bypass pores and reach the output surface successfully. This process is completed using Breadth-First Search to ensure the shortest heat flow path and identify all valid paths without intersection. Here, some grid cells representing single-phase particles have been assigned a heat flow direction attribute to mark the paths traversing them. Third, for those grid cells representing single-phase particles that have not yet been assigned a heat flow direction attribute, their heat flow directions are made to align as much as possible with those of their surrounding cells, thereby merging them into the paths. This approach reasonably simulates changes in the cross-sectional area along heat flow paths. Through these three steps, multiple heat flow paths can be obtained within the cube from the heat flow input surface to the output surface. The thermal resistance of a single path p

can be estimated as:

$$R_p = \frac{1}{\lambda n_1 \delta} + \sum_{i=2}^{N_p} \left[\frac{1}{\lambda n_i \delta} + \frac{2r}{(n_i + n_{i-1}) \delta^2} \right] \quad (14)$$

where N_p is the number of cubic grid cells traversed by path p in the heat transfer direction. The heat conduction can be visualized as the heat flow reaching the output surface after N_p steps of transmission from the input surface. δ denotes the side length of a single cubic grid cell. n_i represents the number of grid cells belonging to path p at the i th step position, which characterizes the change in the cross-sectional area of the heat flow. The total thermal resistance R is the parallel combination of the thermal resistances of all paths, satisfying:

$$\frac{1}{R} = \sum_p \frac{1}{R_p} \quad (15)$$

After averaging multiple simulation runs, the estimated thermal resistance R of the cubic micro-element is $1.61 \times 10^7 \text{ K W}^{-1}$, based on which, the equivalent interfacial thermal resistance can be calculated as $R_e = 1.01 \times 10^{-5} \text{ m}^2 \text{ K W}^{-1}$. This value was used as the input parameter for the FDM to calculate the thermal conductivity of a single particle. Figure S23 illustrates the heat flow paths formed within the micro-element during one simulation run.

Data availability

All data supporting the findings of this study can be found in the article and its Supplementary Information. More detailed primary experimental data are available from the corresponding author upon reasonable request.

Received: 15 September 2025; Accepted: 27 February 2026;

Published online: 18 March 2026

References

- Guo, J. et al. Hypocrystalline ceramic aerogels for thermal insulation at extreme conditions. *Nature* **606**, 909–916 (2022).
- Lu, X. et al. Thermal conductivity of monolithic organic aerogels. *Science* **255**, 971–972 (1992).
- Pang, K. et al. Dome-celled aerogels with ultrahigh-temperature superelasticity over 2273 K. *Science* **389**, 290–294 (2025).
- Xu, X. et al. Double-negative-index ceramic aerogels for thermal superinsulation. *Science* **363**, 723–727 (2019).
- Yu, H. et al. Chemically bonded multi-nanolayer inorganic aerogel with a record-low thermal conductivity in a vacuum. *Natl. Sci. Rev.* **10**, nwad129 (2023).
- Bheekhun, N., Abu Talib, A. R. & Hassan, M. R. Aerogels in aerospace: an overview. *Adv. Mater. Sci. Eng.* **2013**, 406065 (2013).
- Kilincarslan, Ş., Davraz, M. & Akça, M. The effect of pumice as aggregate on the mechanical and thermal properties of foam concrete. *Arab. J. Geosci.* **11**, 289 (2018).
- Koçyigit, F., Kavak Akpınar, E. & Biçer, Y. Experimental and theoretical study for the determination of thermal conductivity of porous building material made with pumice and tragacanth. *J. Adhes. Sci. Technol.* **30**, 2357–2371 (2016).
- Smith, M. et al. The Artemis Program: an overview of NASA's activities to return humans to the moon. In *Proc. IEEE Aerospace Conference* <https://ieeexplore.ieee.org/document/9172323/>.
- Xu, L., Li, H., Pei, Z., Zou, Y. & Wang, C. A brief introduction to the international lunar research station program and the interstellar express mission. *Chin. J. Space Sci.* **42**, 511–513 (2022).
- Li, C., Wang, C., Wei, Y. & Lin, Y. China's present and future lunar exploration program. *Science* **365**, 238–239 (2019).

12. Cremers, C. J., Birkebak, R. C. & Dawson, J. P. Thermal conductivity of fines from Apollo 11. In *Proc. Apollo 11 Lunar Science*, Vol. 3, 2045–2050 (Pergamon Press, 1970).
13. Cremers, C. J. Thermal properties of Apollo 14 fines. *J. Geophys. Res.* **80**, 4466–4470 (1975).
14. Cremers, C. J. & Hsia, H. S. Thermal conductivity and diffusivity of Apollo 15 fines at low density. In *Proc. Lunar Science Conference*, Vol. 4, 2459–2464 (Pergamon Press, 1973).
15. Cremers, C. J. & Hsia, H. S. Thermal conductivity of Apollo 16 lunar fines. In *Proc. Lunar Science Conference*, Vol. 3, 2703–2708 (Pergamon Press, 1974).
16. Keihm, S. J., Peters, K. & Langset, M. G. Apollo 15 measurement of lunar surface brightness temperatures thermal conductivity of the upper 1 1/2 meters of regolith. *Earth Planet. Sci. Lett.* **19**, 337–351 (1973).
17. Marcus, G. & Langseth, J. R. The Apollo 15 lunar heat-flow measurement. *Moon* **4**, 390–410 (1972).
18. Langseth, M. G., Keihm, S. J. & Peters, K. Revised lunar heat-flow values. In *Proc. Lunar Science Conference*, Vol. 7, 474–475 (Pergamon Press, 1976).
19. Keihm, S. J. & Langseth, M. G. Surface brightness temperatures at the Apollo 17 heat flow site—thermal conductivity of the upper 15 cm of regolith. In *Proc. Lunar Science Conference*, Vol. 4, 2503–2513 (Pergamon Press, 1973).
20. Xiao, X. et al. Thermophysical properties of the regolith on the lunar far side revealed by the in-situ temperature probing of the Chang'E-4 mission. *Natl. Sci. Rev.* **9**, nwac175 (2022).
21. Clauser, C. & Huenges, E. Thermal conductivity of rocks and minerals. In *Rock Physics and Phase Relations: A Handbook of Physical Constants* (ed. Ahrens, T. J.) Vol. 3, 105–126 (American Geophysical Union, 1995).
22. Horai, K. Thermal conductivity of rock-forming minerals. *J. Geophys. Res.* **76**, 1278–1308 (1971).
23. Branlund, J. M. & Hofmeister, A. M. Heat transfer in plagioclase feldspars. *Am. Mineral.* **97**, 1145–1154 (2012).
24. Yoneda, A., Yonehara, M. & Osako, M. Anisotropic thermal properties of talc under high temperature and pressure. *Phys. Earth Planet. Inter.* **190**, 10–14 (2012).
25. Horai, K. The effect of interstitial gaseous pressure on the thermal conductivity of a simulated Apollo 12 lunar soil sample. *Phys. Earth Planet. Inter.* **27**, 60–71 (1981).
26. Wood, S. E. A mechanistic model for the thermal conductivity of planetary regolith: 1. The effects of particle shape, composition, cohesion, and compression at depth. *Icarus* **352**, 113964 (2020).
27. Li, S. et al. Formation of lunar surface water associated with high-energy electrons in Earth's magnetotail. *Nat. Astron.* **7**, 1427–1435 (2023).
28. Anand, M. et al. Space weathering on airless planetary bodies: Clues from the lunar mineral hapkeite. *Proc. Natl. Acad. Sci. USA* **101**, 6847–6851 (2004).
29. Hu, S. et al. A dry lunar mantle reservoir for young mare basalts of CE-5. *Nature* **600**, 49–53 (2021).
30. Wu, F. et al. Lunar evolution in light of the CE-5 returned samples. *Annu. Rev. Earth Planet. Sci.* **52**, 159–194 (2024).
31. Zhao, R. et al. Diverse glasses revealed from CE-5 lunar regolith. *Natl. Sci. Rev.* **10**, nwad079 (2023).
32. Zhang, H. et al. Size, morphology, and composition of lunar samples returned by CE-5 mission. *Sci. China Phys. Mech. Astron.* **69**, 229511 (2022).
33. Li, C. et al. Characteristics of the lunar samples returned by the CE-5 mission. *Natl. Sci. Rev.* **9**, nwab188 (2022).
34. Guo, J. et al. Surface microstructures of lunar soil returned by CE-5 mission reveal an intermediate stage in space weathering process. *Sci. Bull.* **67**, 1696–1701 (2022).
35. Heiken, G. Petrology of lunar soils. *Rev. Geophys.* **13**, 567–587 (1975).
36. Cao, Z. et al. Nature of space-weathered rims on CE-5 lunar soil grains. *Earth Planet. Sci. Lett.* **658**, 119327 (2025).
37. Li, C. et al. Impact-driven disproportionation origin of nanophase iron particles in CE-5 lunar soil sample. *Nat. Astron.* **6**, 1156–1162 (2022).
38. Guo, Z. et al. Sub-microscopic magnetite and metallic iron particles formed by eutectic reaction in CE-5 lunar soil. *Nat. Commun.* **13**, 7177 (2022).
39. Zhang, C. et al. Atomic-level structural responses of CE-5 ilmenite to space weathering. *J. Geophys. Res. Planets* **192**, e2024JE008447 (2024).
40. Zhang, Y. et al. Simultaneous electrical and thermal rectification in a monolayer lateral heterojunction. *Science* **67**, 1696–1701 (2022).
41. Wang, H. et al. Experimental study of thermal rectification in suspended monolayer graphene. *Nat. Commun.* **8**, 15843 (2017).
42. Zheng, J. et al. Precise characterization of thermal conductivity and interfacial thermal resistance of individual polymer microparticle. *Int. J. Heat Mass Transfer* **232**, 125880 (2024).
43. Zhang, Z. M. & Luby, S. *Nano/Microscale Heat Transfer* (McGraw-Hill, 2007).
44. Kittel, C. Interpretation of the thermal conductivity of glasses. *Phys. Rev.* **75**, 972–974 (1949).
45. Shabbir, G., Maqsood, A. & Majid, C. A. Thermophysical properties of consolidated porous rocks. *J. Phys. D Appl. Phys.* **33**, 658–662 (2000).
46. Delano, J. W., Hughes, S. S. & Schmitt, R. A. Collaborative study of the Apollo 15 pristine yellow/brown glasses: an interim report. *Lunar Planet. Sci.* **17**, 172–173 (1986).
47. Heiken, G. H., McKay, D. S. & Brown, R. W. Lunar deposits of possible pyroclastic origin. *Geochim. Cosmochim. Acta* **38**, 1703–1718 (1974).
48. Merabia, S. & Termentzidis, K. Thermal conductance at the interface between crystals using equilibrium and nonequilibrium molecular dynamics. *Phys. Rev. B* **86**, 094303 (2012).
49. Goncalves, S. & Bonadeo, H. Vibrational densities of states from molecular-dynamics calculations. *Phys. Rev. B* **46**, 12019 (1992).
50. Green, M. S. Markoff random processes and the statistical mechanics of time-dependent phenomena. *J. Chem. Phys.* **20**, 1281–1295 (1952).
51. Kubo, R. Statistical-Mechanical theory of irreversible processes. I. General theory and simple applications to magnetic and conduction problems. *J. Phys. Soc. Jpn.* **12**, 570–586 (1957).
52. Zakharov, A. V. et al. Physical processes leading to surface erosion and dust particles dynamics of airless bodies. *Phys. Plasmas* **29**, 110501 (2022).
53. Xu, Y. et al. High abundance of solar wind-derived water in lunar soils from the middle latitude. *Proc. Natl. Acad. Sci. USA* **119**, e2214395119 (2022).
54. He, H. et al. A solar wind-derived water reservoir on the Moon hosted by impact glass beads. *Nat. Geosci.* **16**, 294–300 (2023).
55. Dubinskii, A. Y. & Popel, S. I. Water formation in the lunar regolith. *Cosmic Res.* **57**, 79–84 (2019).
56. Audoit, J. et al. Thermal, mechanical and dielectric behaviour of poly (aryl ether ketone) with low melting temperature. *J. Therm. Anal. Calorim.* **135**, 2147–2157 (2019).
57. Edalatpour, S. & Francoeur, M. Size effect on the emissivity of thin films. *J. Quant. Spectrosc. Radiat. Transfer* **118**, 75–85 (2013).
58. McCloy, J. S., Sundaram, S. K., Matyas, J. & Woskov, P. P. Simultaneous measurement of temperature and emissivity of lunar regolith simulant using dual-channel millimeter-wave radiometry. *Rev. Sci. Instrum.* **82**, 054703 (2011).
59. Thompson, A. P. et al. LAMMPS—a flexible simulation tool for particle-based materials modeling at the atomic, meso, and continuum scales. *Comput. Phys. Commun.* **271**, 108171 (2022).
60. Plimpton, S. Fast parallel algorithms for short-range molecular dynamics. *J. Comput. Phys.* **117**, 1–19 (1995).

61. Cygan, R. T., Liang, J. J. & Kalinichev, A. G. Molecular models of hydroxide, oxyhydroxide, and clay phases and the development of a general force field. *J. Phys. Chem. B* **108**, 1255–1266 (2004).
62. Van Beest, B. W. H., Kramer, G. J. & Van Santen, R. A. Force fields for silicas and aluminophosphates based on ab initio calculations. *Phys. Rev. Lett.* **64**, 1955 (1990).
63. Vollmayr, K., Kob, W. & Binder, K. Cooling-rate effects in amorphous silica: A computer-simulation study. *Phys. Rev. B* **54**, 15808 (1996).
64. McGaughey, A. J. H. & Kaviany, M. J. I. J. Thermal conductivity decomposition and analysis using molecular dynamics simulations: Part II. Complex silica structures. *Int. J. Heat Mass Transfer* **47**, 1799–1816 (2004).
65. Roder, A., Kob, W. & Binder, K. Structure and dynamics of amorphous silica surfaces. *J. Chem. Phys.* **114**, 7602–7614 (2001).
66. Mahajan, S. S., Subbarayan, G. & Sammakia, B. G. Estimating thermal conductivity of amorphous silica nanoparticles and nanowires using molecular dynamics simulations. *Phys. Rev. E Stat. Nonlinear Soft Matter Phys.* **76**, 056701 (2007).
67. Nosé, S. A unified formulation of the constant temperature molecular dynamics methods. *J. Chem. Phys.* **81**, 511–519 (1984).

Acknowledgements

The authors thank all the staff of the Chang'e lunar exploration project for their hard work, and the China National Space Administration (CNSA) for providing access to the Lunar samples CE5C0400. This work is supported by the National Natural Science Foundation of China (grant nos. 52425601, 42441804, 52327809) and the National Key Research and Development Program of China (grant nos. 2021YFA0717200, 2023YFB4404100).

Author contributions

G.Z. and H.W. initiated and supervised the study. Z.T., J.Z., G.Z., and H.W. designed the overall experimental approach. Y.L. and P.Z. supervised the morphological and mineralogical characterization. Z.T., R.P., Q.Z., X.L., Yiwei Liu, S.Y., and G.L. conducted morphological and mineralogical measurements. G.Z. and P.Z. designed the 3D reconstruction methods for lunar particles. Z.T., Q.Z., X.L., Yiwei Liu, G.Z., and P.Z. conducted the 3D reconstruction. H.W. and B.C. supervised the thermal conductivity measurement of lunar particles. H.W., J.Z., and B.C. designed and fabricated the H-type device. H.W., J.Z., and B.C. completed the transfer of single particle samples with help from G.Z., Y.L., and J.L. J.Z., H.W., and B.C. measured the thermal conductivities of the samples and analyzed the experimental data. Y.L. performed the nanoscale mineral interface characterization within individual particles. B.C. supervised the MD calculation. Y.C., J.Z., H.W., and B.C. conducted the MD calculations. G.Z. supervised the FDM calculation. G.Z., Z.T., J.Z., and H.W. conducted the FDM

calculations. P.Z. provisioned the calculation and computing resources. Y.L., J.L., and Z.O. contributed to the mineralogy and space weathering discussions. Y.L., J.L., and Z.O. provided background information on the samples. G.Z., H.W., B.C., and P.Z. supplied the commercial support. Z.T. and J.Z. wrote the manuscript. Z.T., J.Z., H.W., G.Z., and Y.L. revised the manuscript with contributions from all authors. G.Z. served as the primary corresponding author of this work and was responsible for editorial communication.

Competing interests

The authors declare no competing interests.

Additional information

Supplementary information The online version contains supplementary material available at <https://doi.org/10.1038/s43246-026-01126-9>.

Correspondence and requests for materials should be addressed to Haidong Wang, Guang Zhang, Yang Li, Bingyang Cao or Peng Zhang.

Peer review information *Communications Materials* thanks Beatriz Merillas, Sebastien Verkercke, and the other, anonymous, reviewers for their contribution to the peer review of this work. A peer review file is available.

Reprints and permissions information is available at <http://www.nature.com/reprints>

Publisher's note Springer Nature remains neutral with regard to jurisdictional claims in published maps and institutional affiliations.

Open Access This article is licensed under a Creative Commons Attribution 4.0 International License, which permits use, sharing, adaptation, distribution and reproduction in any medium or format, as long as you give appropriate credit to the original author(s) and the source, provide a link to the Creative Commons licence, and indicate if changes were made. The images or other third party material in this article are included in the article's Creative Commons licence, unless indicated otherwise in a credit line to the material. If material is not included in the article's Creative Commons licence and your intended use is not permitted by statutory regulation or exceeds the permitted use, you will need to obtain permission directly from the copyright holder. To view a copy of this licence, visit <http://creativecommons.org/licenses/by/4.0/>.

© The Author(s) 2026